ROYAL SOCIETY
OF CHEMISTRY

PAPER

Check for updates

Aminated graphene quantum dots/CdS nanobelts for enhanced photocatalytic degradation of RhB dye under visible light†

Xiangfeng Lin, [ID] *[ab] Yu Chen,[ab] Diwen Zhou,[c] Menglin Chen,*[ab] Weixia Liang*[d] and Huazhang Guo*[c]

CdS nanoparticles have wide applications as photocatalysts for degradation of organic pollutants, but due to their limited turnover number and off-pathway charge recombination processes, their degradation efficiency is low. Herein, aminated graphene quantum dots/CdS (GQDs/CdS) nanobelts were successfully fabricated by solvothermal and hydrothermal processes. The prepared GQDs/CdS were characterized by physical methods to investigate their structure, morphology, optical properties, specific surface area, element composition, and chemical state. GQDs/CdS materials promoted efficient charge separation, and showed high efficiency in the photocatalytic degradation of the organic dye Rhodamine B (RhB) under visible light. The degradation efficiency of RhB samples over 0.05 g of catalysts reached 97.40% after 150 min, a much higher efficiency in comparison to pure CdS. Electron paramagnetic resonance (EPR) spectroscopy provided direct evidence for ·OH and ·O$_2^-$ as the reactive oxidative species using DMPO as a spin trap. Consistent with the experimental results, a possible mechanism of RhB photocatalytic degradation by GQDs/CdS under visible light was proposed. This work may provide environmentally friendly photocatalysts for degrading organic dyes and purifying water.

1. Introduction

Organic dyes are widely used in the manufacturing of consumable goods (textiles, glass, paper products, *etc.*) in modern society. Their prevalence in all facets of life is underscored by estimations that the global organic dyes market will reach over $5.1 billion by the end of 2027.[1] Among numerous dyes, RhB is one of the most widely-used organic dyes in printing and in textiles. In spite of its ubiquity, RhB is harmful to human health: exposure to RhB can cause skin irritation, vomiting, and nausea.[2] The artificial organic dyes exhibit high toxicity, low biodegradability, chemical stability and difficult degradation, even at low concentrations; these dyes are dangerous and seriously threaten human health and the ecological environment.[3] At present, manufacturing processes release a large amount of dye in the wastewater. An estimated

10–20% of dyes run off into the treated wastewater because of inefficiencies in the coloring process.[4] Presently, different treatment technologies such as adsorption, biological oxidation, oxidation by chemical reagents, and flocculation/coagulation are extensively used to treat dyes in wastewater.[3] However, these technologies have their own limitations, such as selective adsorption, long processing time, large area occupied, low removal efficiency, and noxious byproducts.[5] These limitations provide a driving force to explore new techniques to efficiently eliminate dye contaminants from various sources. Photodegradation has attracted great attention for organic wastewater as it is economical, green, and can operate at high removal efficiencies. Moreover, some photocatalysts can use natural, visible light, as opposed to artificial light.[4,5] Many semiconductor catalysts such as metal oxides (TiO$_2$, ZnO, WO$_3$, CeO$_2$, *etc.*), metal sulfides (ZnS, CdS, Mo$_2$S, Bi$_2$S$_3$, *etc.*), ternary compounds (BaTiO$_3$, Bi$_2$WO$_6$, BiVO$_4$, *etc.*), and non-metal semiconductors (g-C$_3$N$_4$, black phosphorus, *etc.*) have shown outstanding performance in photocatalytic degradation of organic pollutants.[6–12]

CdS is a semiconductor with a relatively narrow energy band (2.4 eV), allowing it to be driven by sunlight and used as a visible light photocatalyst. The conduction band position of CdS is sufficiently negative to allow the transfer of the valence electrons from the nanoparticle surface to adsorbed molecules.[13] In recent years, CdS semiconductors have gained attention due to its low cost, easy portability, and high electronic mobility.[14,15]

[a]School of Environment and Resource, Guangxi Normal University, Guilin 541004, PR China. E-mail: mlchen99@163.com; 310976435@qq.com

[b]Guangxi Key Laboratory of Environmental Processes and Remediation in Ecologically Fragile Regions, China

[c]School of Environmental and Chemical Engineering, Shanghai University, Shanghai 200444, PR China. E-mail: guohuazhang@shu.edu.cn

[d]School of Medicine and Health, Guangxi Vocational & Technical Institute of Industry, Nanning 530001, China. E-mail: liangwxabc@163.com

† Electronic supplementary information (ESI) available: Fig. S1: SEM image of CdS nanobelt. Fig. S2: SEM image of CdS-4. Fig. S3: high-resolution XPS spectra of C 1s of CdS-4 composite. See DOI: https://doi.org/10.1039/d3ra06454a

However, pure CdS materials are not stable and tend to aggregate, which reduces the specific surface area, leading to lower overall reactivity.[16] Additionally, CdS is sensitive to severe photodegradation, leading to rapid recombination of photo-generated electron–hole pairs.[17] This further limits the overall reactivity of CdS-based catalysts. To solve these problems, modification of CdS morphologies have been developed to enhance the photocatalyst efficiency. These strategies include changing the morphology of CdS from bulk material to nano-spheres (either mesoporous or nanorods structures),[18–22] and doping with metal/non-metal elements such as Ag, graphene quantum dots (GQDs), g-C$_3$N$_4$,[23–25] and other semiconductors like TiO$_2$, WO$_3$, MoS$_2$.[26–28] Among these modifications, GQDs are zero-dimensional carbon nanomaterials that are low cost, non-toxic, have excellent optical performance, are biocompatible, and amenable to surface modifications.[29] Furthermore, GQDs show very strong visible light absorption properties, have tunable bandgaps, and possess superior photo-stability.[24] When GQDs are joined with CdS as GQDs/CdS composites, the GQDs act as the effective electron transfer mediator to improve charge separation efficiency, while CdS is the photocatalytic active center that harvests light and drive various catalytic processes.[24] Therefore, GQDs and GQD-based materials such as GQDs/CdS composites have been used in various applications such as CO$_2$ reduction photocatalysts,[30] environmental monitoring devices,[31] photocatalysts for the photodegradation of organic pollutants,[32] H$_2$ or H$_2$O$_2$ evolution catalysts[24,33,34] and bioimaging markers.[35]

Although GQDs/CdS composites have been used in the visible light-driven degradation of organic pollutants, the ability of aminated GQDs/CdS nanobelts to drive photocatalytic degradation of RhB has not yet been thoroughly studied. In this work, we successfully prepared a GQDs/CdS photocatalyst *via* three simple process: (1) solvothermal synthesis of CdS nanowires, (2) hydrothermal synthesis of GQDs, (3) preparation of GQDs/CdS composites by physical mixing of GQDs and CdS. The structures, morphologies, and optical properties were characterized by physical methods. GQDs/CdS composites showed high photocatalytic performance in degradation of high concentrations of RhB, with visible light as light source. Based on the above results, a possible mechanism of the RhB degradation over GQDs/CdS composites was also proposed. The load of GQDs promoted the separation of carriers and charge transfer efficiency, accelerating the visible light degradation of dye RhB. This study would facilitate our insight into a new strategies to improve the effectiveness of water purification.

2. Experimental

2.1. Chemicals and reagents

Trinitropyrene (purity: 98%) and RhB were purchased from TCI (Shanghai, China). Cd(NO$_3$)$_2$, thiourea, ethylenediamine, and ammonia were analytically pure and supplied by Sinopharm Chemical Reagent Co., Ltd (Shanghai, China). All chemicals and reagents were used without further purification. Deionized water was used in all experiments.

2.2. Synthesis of CdS nanobelts

The CdS nanobelts were synthesized by a simple solvothermal process. The typical experiment was as follows: 2.5 g Cd(NO$_3$)$_2$ and 2 g thiourea were mixed. Next, 50 mL ethylenediamine was added into the above mixture and stirred uniformly, then, the well-mixed liquid was transferred into a Teflon-lined stainless steel autoclave, and reacted at 200 °C for 60 h. After cooling naturally to room temperature, the products were washed with water and centrifuged several times until the centrifugal effluent was neutral. Finally, the sediment was washed with absolute ethanol, dried, resulting in CdS nanobelts as a fine yellow powder.

2.3. Synthesis of aminated GQDs

The low cost hydrocarbon pyrene (C$_{16}$H$_{10}$) was used as precursor of graphene quantum dots. 2.0 g of pyrene dissolved in to 160 mL HNO$_3$ and stirred with a magnetic stir under reflux at 80 °C for 12 h. Then, the solution was left to cool to room temperature, after which the mixture was diluted with distilled water. Next, the solution was filtered with a 0.22 µm microporous membrane to remove the liquid, and washed with water three times. The yellow product was 1,3,6-trinitropyrene. 0.1 g of 1, 3, 6-trinitropyrene was uniformly dispersed in 10 mL deionized water through ultrasonication, then 1 mL of ammonia was slowly added dropwise into the above solution while stirring. Then, the suspension was transferred into a Teflon-lined stainless steel autoclave, and reacted at 200 °C for 12 h. Finally, the aminated GQDs in solution were obtained by filtering the product through a 0.22 µm microporous membrane to remove traces of insoluble impurities.[36]

2.4. Preparation of aminated GQDs/CdS composites

The aminated GQDs/CdS composite was prepared by a simple hydrothermal deposition. 0.5 g of CdS was dispersed into different amounts of the aminated GQDs solution *via* ultrasonication to form a suspension, then was heated under intense magnetic stirring until the solvent completely volatilized. The yellow deposition was washed with water and absolute ethanol, dried, leaving behind the aminated GQDs/CdS composite. The weight ratios of aminated GQDs to CdS were 0%, 0.5%, 1%, 2%, 3%, 4%, and they were named CdS, CdS-0.5, CdS-1, CdS-2, CdS-3 and CdS-4, respectively. Previous literature reveals that NH$_2$-functionalized GQDs improve CO$_2$-to-CH$_4$ selectivity effectively.[37] Here the aim of amination of GQDs/CdS is to achieve efficient charge carrier separation and transfer, enhancing the photocatalytic activity of catalysts.[38]

2.5. Characterization

The structure and crystallinity of as-prepared catalysts were analyzed by a D8 Bruker X-ray diffractometer (Bruker Corporation, Billerica, USA). The X-ray photoelectron spectroscopy (XPS) measurements were obtained by a PHI 5000C ESCA System X-ray photoelectron spectroscopy (Physical Electronic Corporation, Tumwater, USA). Nitrogen adsorption–desorption

measurements were carried out by an automated gas sorption analyzer (QuadraSorb SI, Quantachrome Corporation, Boynton Beach, USA). A Hitachi U4100 UV-vis spectrophotometer equipped with an integrating sphere (Hitachi Ltd., Tokyo, Japan) was used to record the UV-vis diffuse reflectance spectra. The morphology of catalysts was investigated by A Quanta 200 FEG scanning electron microscope (SEM, FEI Corporation, Hillsboro, USA). Electron paramagnetic resonance (EPR) measurement was conducted in a JEOL JES FA200 EPR Spectrometer (JEOL Ltd., Akishima, Japan). The concentration of dyes were measured by UV-vis spectrophotometer (TU-1901, Beijing Purkinje General Instrument Co., Ltd., Beijing, China). Transmission electron microscopy (TEM) measurements were investigated by transmission electron microscope (Hitachi HT7700, Hitachi Limited, Japan). Electrochemical impedance spectroscopy (EIS) analyses were performed in the Autolab (AUT88032) electrochemical workstation (Metrohm, Switzerland).

2.6. Photocatalytic degradation of RhB dye

The RhB dye was used as a simulated pollutant to assay the photocatalytic activity of the synthesized catalysts under visible light. Briefly, a certain amount of aminated GQDs/CdS composites were mixed with 50 mL of RhB dye solution (initial concentration: 20–150 mg L^{-1}), the solution was adjusted to required pH range and stirred in the dark for 1 h to achieve the adsorption/desorption equilibrium between dye and catalyst. Then, the catalyst/dye mixture was transferred onto a multi-position photochemical reaction system (Zhongjiao Jinyuan Technology Co., Ltd., Beijing, China) and irradiated by a xenon lamp. The sample mixtures were collected for an interval time and filtered with a 0.22 μm microporous membrane. Finally, the concentration of RhB in the liquid samples were measured by UV-vis spectrophotometer to calculate overall degradation of RhB dye. The reusability experiment was carried out under conditions of: catalyst dosage: 0.05 g, RhB concentration: 50 mg L^{-1}, pH: 3.0 and reaction time: 150 min. When the catalytic reaction was completed, the suspension containing catalyst and residual dye was centrifuged for 15 min, the remaining solution was discarded. Then the catalyst was transferred into reaction tube with the help of stirring rod and RhB solution (rinse the catalyst). Then the next round of reaction was performed after adsorption equilibrium.

The removal efficiency was calculated by using eqn (1).

$$\text{Removal efficiency (\%)} = (1 - C/C_o) \times 100 \quad (1)$$

The reaction kinetics for RhB over CdS with different GQDs loading were fitted by pseudo first-order kinetics model, which was as the following eqn (2).

$$-\ln(C/C_o) = k_1 t \quad (2)$$

where C_o and C are the initial concentration and the concentration at a certain interval time, respectively, k_1 is the first order rate constant.

3. Results and discussion

3.1. Characterization

3.1.1 Structual characterization and chemical composition.
The GQDs/CdS composite was synthesized by a simple hydrothermal deposition. Different the weight ratios of aminated GQDs to CdS nanobelt (0, 0.5%, 1%, 2%, 3%, 4%) were considered in the preparation of GQDs/CdS composite under the same condition. The aminated GQDs was a Janus, which was not only beneficial to the dispersion and hydrophilicity of GQDs with amino group, but also π–π stacking of GQD and CdS nanobelt is more conducive to the composite. The chemical structure of pure CdS and CdS-4 were checked by XRD measurement, as shown in Fig. 1a. The pure CdS shows characteristic diffraction peaks at 2θ values of 25.18°, 26.83°, 28.51°, 36.95°, 44.09°, 48.20°, 51.18°, 52.19°, 53.26°, 58.73°, 67.17°, 69.68°, 71.22°, 72.77°, 75.86°, which can be well indexed to the (100), (002), (101), (102), (110), (103), (200), (201), (004), (202), (203), (210), (211), (114) and (212) crystal planes of hexagonal structure with space group 'P6$_3$mc', assigned to the standard JCPDS card no. 65-3414.[39] These peaks are in good agreement with the ref. 39 and 40 upon the addition of GQDs. It is observed that some diffraction intensity of peaks is increased or decreased slightly compared to CdS sample. However, the characteristic diffraction peaks from GQDs cannot be detected due to the small amount and/or high dispersion and relatively low diffraction intensity of GQDs.[24,41]

The XPS analysis was used to investigate the chemical composition and chemical interactions between GQDs and CdS. Fig. 1b shows the XPS survey spectrum of CdS-4, which reveals that strong signals characteristic of the Cd 3d, S 2p, C 1s, N 1s, and O 1s electrons that were detected from the surface of sample. The signals of Cd 3d and S 2p electrons come from CdS, whereas C 1s and O 1s signals originate from GQDs.[24] The XPS of Cd 3d can be deconvoluted into two peaks at 406.14 eV and 412.96 eV, associated with the Cd 3d$_{5/2}$ and Cd 3d$_{3/2}$ configurations, respectively (Fig. 1c). Fig. 1d shows two peaks at 162.20 eV and 163.66 eV, assigned to the S 2p$_{3/2}$ and S 2p$_{1/2}$ electrons, respectively, which are in agreement with a typical value for metal sulfides.[42,43] The C 1s spectra can be fitted by three characteristic peaks, which locate at 285.60, 288.0, and 289.60 eV, respectively. They are assigned to the C–C/C=C, C–N/C–O, and C=O binding modes, respectively (Fig. S3†).[44–46] In Fig. 1e, the high-resolution XPS spectra of O 1s can be separated into C–O[47] and C=O at 533.04 and 534.74 eV.

3.1.2 Morphology characterization.
The morphology of GQDs/CdS composites were characterized by SEM and TEM. It is observed that the morphology of CdS is nanobelt with diameter of about 40 nm, and the length is up to several microns (Fig. S1†). Compared with glaze surface of the pure CdS nanobelts, after modification by GQDs, the surface of CdS-4 becomes rougher (Fig. S2†), some fine particles cover the surface of the nanobelts, which may be the role of GQD as Janus. Notably, GQDs/CdS composites with such structure may be easier to achieve effective charge carrier separation and transfer.
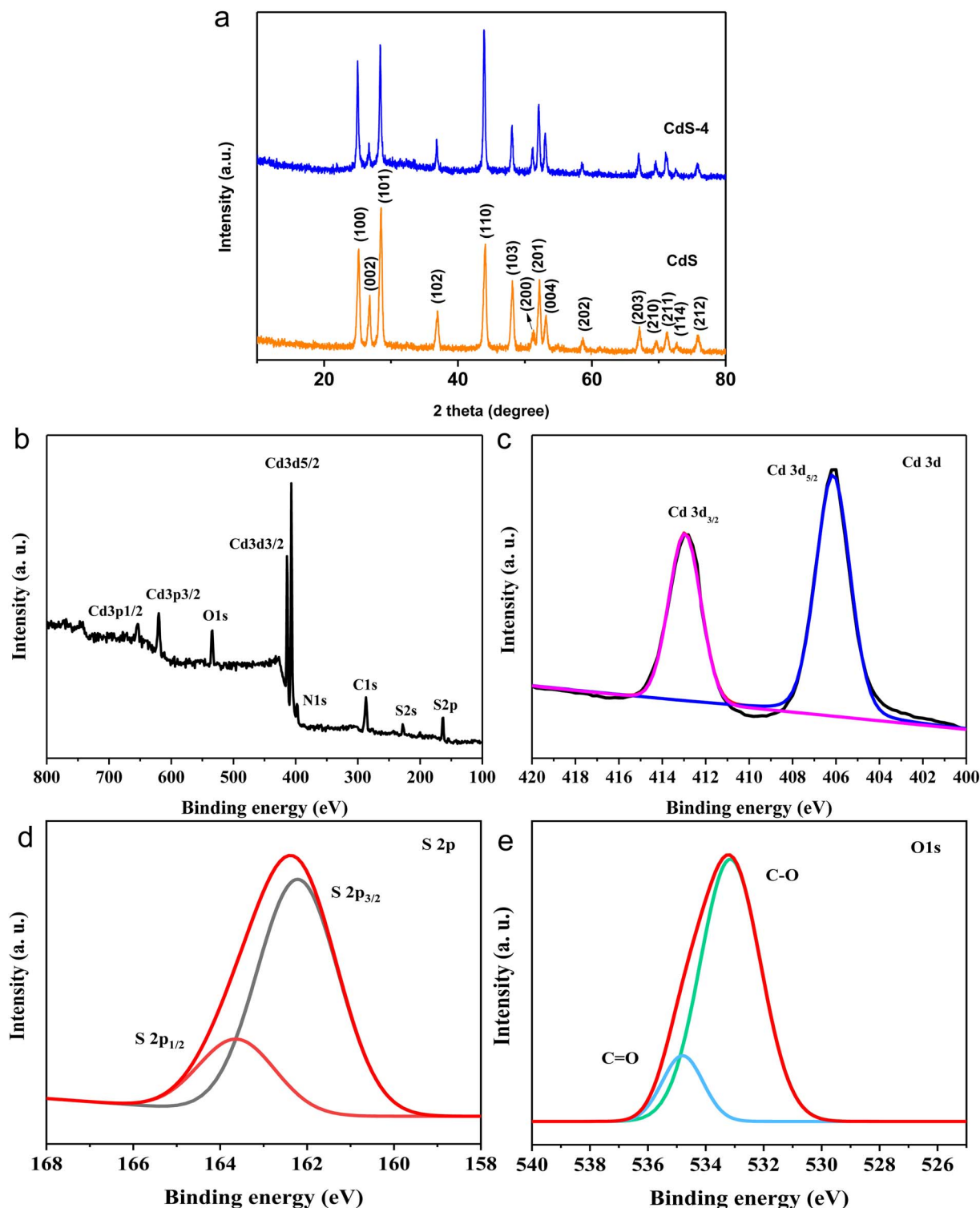
Fig. 1 (a) XRD pattern of CdS and CdS-4. (b) XPS survey spectrum, (c) high-resolution XPS spectrum of Cd 3d, (d) high-resolution XPS spectra of S 2p, (e) high-resolution XPS spectra of O 1s of CdS-4.

The TEM images of these samples are shown in Fig. 2. The as-synthesized amination-GQDs are uniform and mono-dispersed nanodots, their average lateral sizes are 2.53 nm (Fig. 2a). The TEM image of CdS exhibits nanobelt morphology with length in the range from 0.18 up to several microns

(Fig. 2b). After loading by different amounts of GQDs, the diameter of these samples is larger than that of CdS, but their length becomes shorter (Fig. 2c–f).

3.1.3 BET and UV-vis diffuse reflectance analysis. Fig. 3a and b show the N_2 adsorption–desorption isotherm curves and
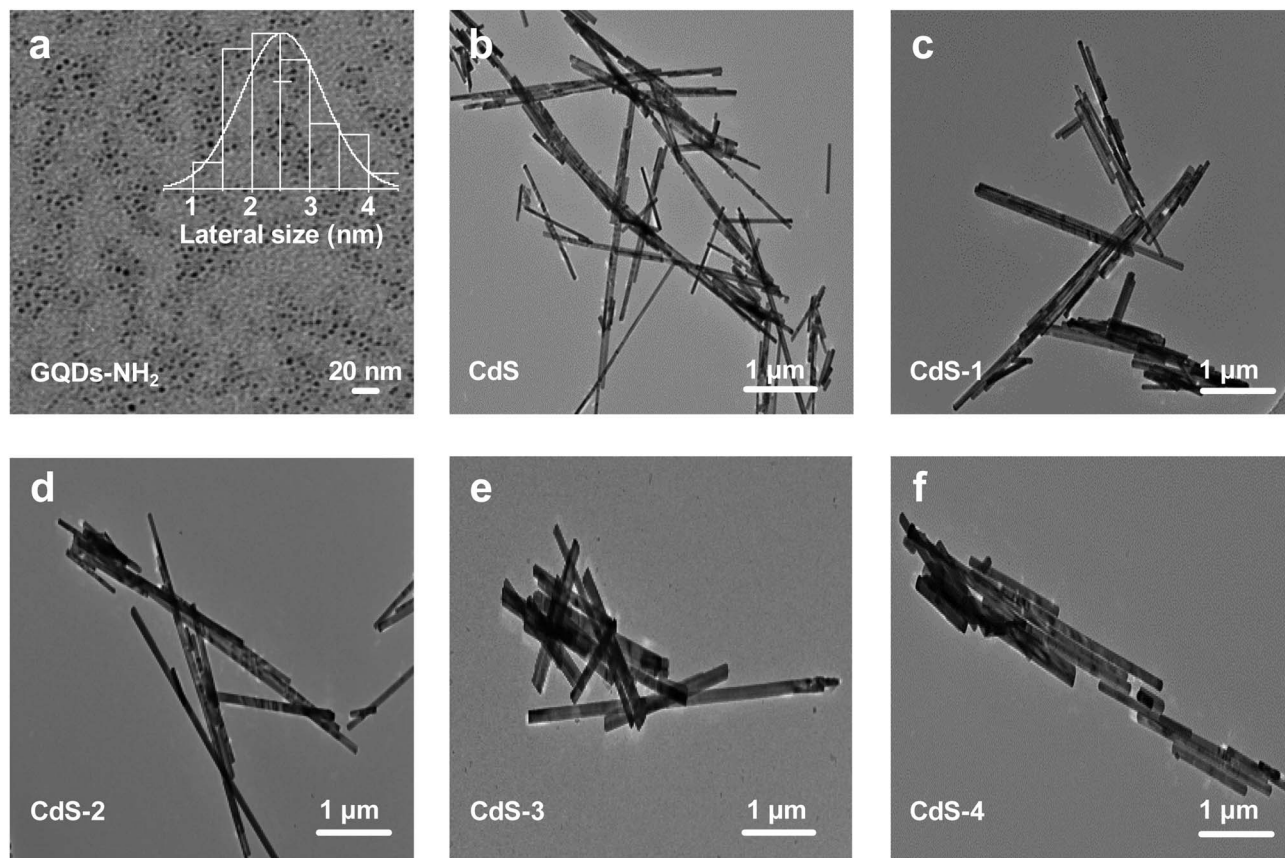
Fig. 2   TEM images of as-prepared samples ((a) aminated GQDs, (b) CdS, (c) CdS-1, (d) CdS-2, (e) CdS-3, (f) CdS-4).

the corresponding pore diameter distribution curve of CdS and CdS-4. Both of them exhibit type IV isotherms with type H3 hysteresis loop (Fig. 3a), demonstrating that the samples contain mesoporous structures, which could form in gaps between stacked nanobelts. The CdS shows hysteresis between 0.88–0.95 relative pressure, while in the case of CdS-4, hysteresis in the N_2 adsorption/desorption occurs across a wider range 0.25–0.98P/P_0. The S_{BET} of CdS-4 (13.33 m^2 g^{-1}) is smaller than for CdS (22.30 m^2 g^{-1}), possibly because the doped GQDs occupy some fraction of the mesoporous structures. However, as shown below, the results of dye degradation by these

photocatalysts, suggest that the specific surface area is not the main factor affecting catalyst activity.[42] The Fig. 3b displays that the majority sizes of the pore in two samples are mainly in the range of 3.4–10 nm.

To investigate the optical properties of the as-prepared catalysts, UV-vis diffuse reflectance spectra (DRS) of the two samples were measured, and are presented in Fig. 3c. The absorption wavelengths of CdS and CdS-4 are both mainly concentrated in the 200–500 nm region. But there are differences in the absorption boundary, with edges at about 539 nm (CdS), 520 nm (CdS-4), respectively. This shift may be due to
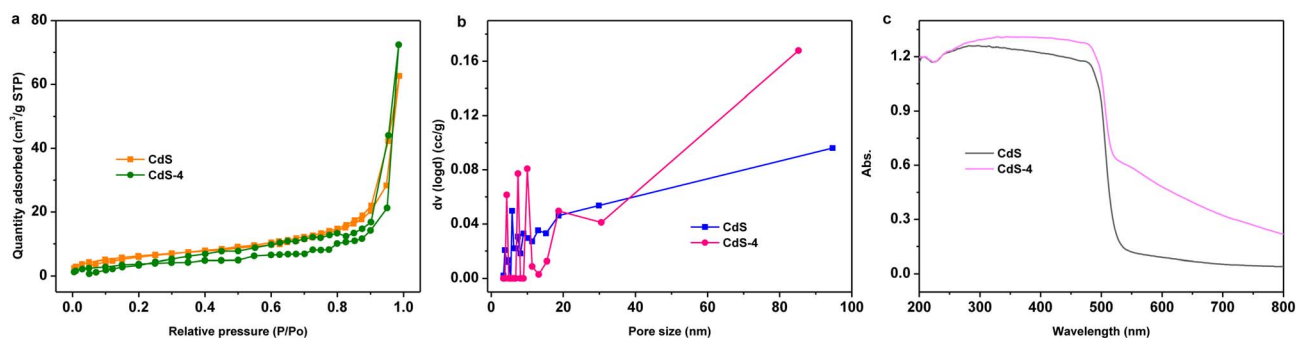

Fig. 3   (a) N_2 adsorption–desorption isotherm curves, (b) the corresponding pore diameter distribution curve, (c) UV-vis diffuse reflectance spectra of CdS and CdS-4.

effects from GQDs doped into the CdS. Furthermore, the peak of CdS-4 is red shifted, and there is enhanced absorption in the 520–800 nm region relative to pure CdS, indicating that introduction of GQDs has improved the overall optical response, consistent with previous results.[24]

3.2. Photocatalytic activity

3.2.1 Effect of GQDs loading on photocatalytic performance. The photocatalytic performance of GQDs/CdS was evaluated by monitoring the photocatalytic degradation of RhB under visible light. Fig. 4a shows the consumption of RhB as a function of time for CdS loaded with different amounts of GQDs. It is observed that the removal of dye by various GQDs/CdS samples includes the dark adsorption and the catalytic degradation process. After mixing the RhB with the various catalysts for 1 h in dark to reach adsorption equilibrium, 30%, 34.9%, 33.2%, 36.2%, 35.2% and 38.0% of RhB were adsorbed by CdS, CdS-0.5, CdS-1, CdS-2, CdS-3 and CdS-4, respectively. After irradiation of 150 min, CdS shows the lowest activity for RhB degradation with a final degradation efficiency of 44.8%. Pure CdS has a propensity for rapid charge recombination of electron–hole pairs, favoring the backward reaction and disfavoring catalysis. Additionally, it has been shown that only a minority of the electron–hole pairs participate in the photocatalytic reaction, and the large over potential on the surface of CdS also disfavor on-pathway catalysis.[39,48,49] The results indicate that there is a general trend of increasing RhB degradation efficiency with increasing loading of GQDs. The CdS-4 sample exhibits the highest dye degradation efficiency of 74.4%, which is 1.6 times higher than that of pure CdS. These results indicate that the combination of GQDs and CdS can enhance the overall catalytic activity.

The reaction kinetics for RhB over CdS with different GQDs loading were calculated. The fitting results (Fig. 4b) are consistent with pseudo first-order kinetics model. The kinetic rate of CdS-4 is the highest (0.00598 min^{-1}), which proves that appropriate loading amounts of aminated GQDs can effectively enhance the utilization of visible light and further improve the photocatalytic performance of the catalyst.

3.2.2 Effect of pH on photocatalytic performance. pH plays a key role in aqueous-based reactions because it can affect surface–surface interactions between catalysts and substrates, *via* the protonation state of the functional groups of pollutant molecules and surface charges of catalyst, which alter the overall adsorption and subsequent photodegradation behavior.[50] The influence of pH values on the degradation of RhB over CdS-4 was investigated by measuring degradation efficiency over a pH range of 3 to 9 in solution. The results are highlighted in Fig. 5a. The removal efficiency of RhB after 150 min slowly decreases with increasing pH: 98.48% (pH 2.99), 73.75% (pH 4.97), 56.89% (pH 7.02) and 54.39% (pH 9.01), respectively. It is apparent that the RhB removal efficiency is higher under acidic conditions than that under basic environments. This indicates that RhB photo-degradation is more favorable under acidic conditions. This could be due to stronger RhB adsorption with the GQDs/CdS catalysts. The azo functional group structure of RhB is positively charged in aqueous solution, while the carboxylic acid group is deprotonated at basic pH, forming a zwitterion. At low pH values, the carboxylate group is protonated, giving RhB an overall positive charge, promoting the adsorption of dye to catalyst, and thereby promoting the photocatalytic reaction.[51] When the pH values is increased to 7 and 9, the carboxylate group of RhB dye is deprotonated to the negatively charged –COO^{-} state,[52,53] which forms a stronger electrostatic repulsion between RhB and the photocatalyst, as a result, the adsorption capacity of dye on the catalyst is reduced, and in turn limiting catalytic degradation of the dye.[54]

The comparison of pH value before and after reaction is displayed in Fig. 5b. In the CdS system, it can be seen that the pH values are all about 6 after reaction when the initial pH varies from 4.97 to 9.01. However, when the initial pH value is 2.99, it is almost unchanged after reaction, which is 3.03. In the case of CdS-4 system, after reaction, the pH values of the
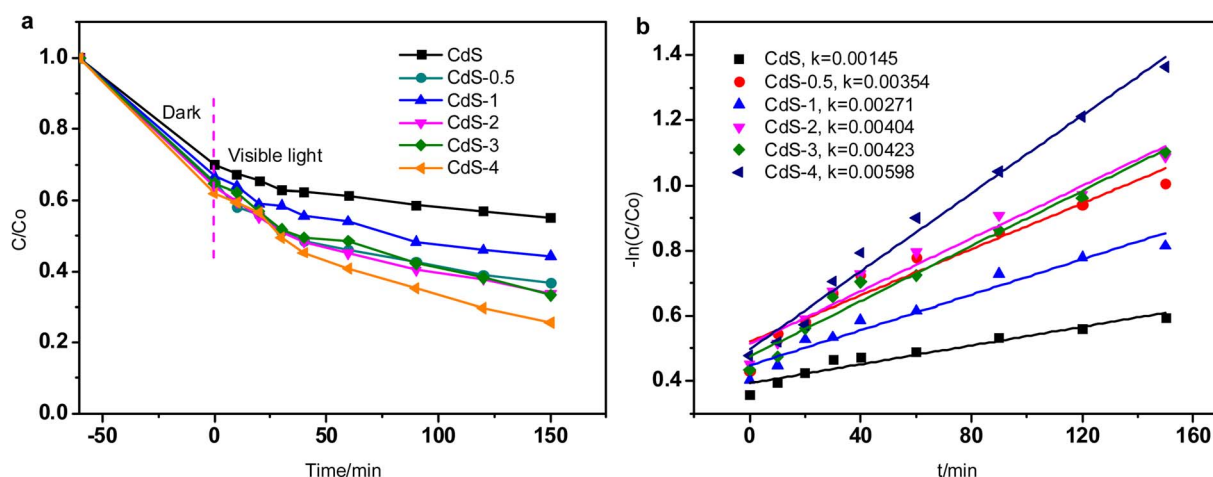

Fig. 4 (a) Effect of GQDs loading over CdS on photocatalytic performance, (b) kinetic simulations (dosage: 0.03 g, pH 7.0, initial concentration: 50 mg L^{-1}).
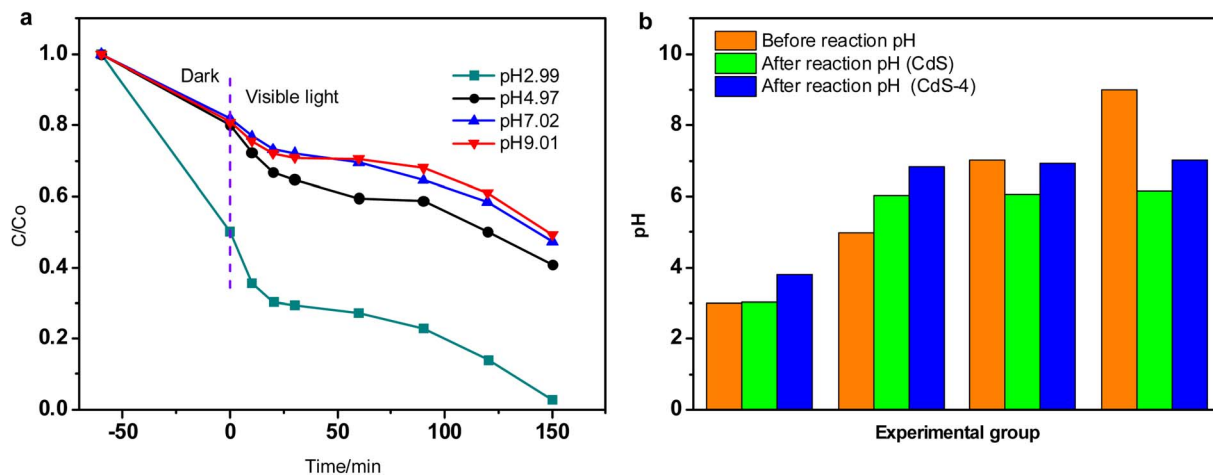
Fig. 5 (a) Effect of pH value on RhB degradation, (b) comparison of pH value before and after reaction (dosage: 0.05 g, initial concentration: 50 mg L^{-1}).

remaining solution are 3.79, 6.84, 6.93 and 7.03, while their corresponding initial pH values are 2.99, 4.97, 7.02 and 9.01, respectively. These results suggest that the amino-GQDs plays an important role in increasing pH at strong acid condition, or helping to form a pH neutral environment when the initial pH varies in range of 5.0–9.0, but the causes for these phenomenons still need to be further explored.

3.2.3 Effect of catalyst dosage and initial concentration of RhB on photocatalytic performance. The effect of increasing amounts of catalyst CdS-4 on the RhB removal rate is shown in Fig. 6a (condition: pH 3.0, initial concentration: 50 mg L^{-1}). After the first 20 min, the larger amounts of catalyst improves the photocatalytic activity of the CdS-4: degradation efficiency of RhB are 62.6%, 63.8% and 68.5%, for 0.05 g, 0.1 g, and 0.2 g catalysts, respectively. With prolonged reaction time, the dye photodegradation efficiency increases with the decrease of catalysts used. After irradiation for 150 min, the degradation efficiency of RhB over 0.2, 0.1 and 0.05 g of catalysts reach 90.25%, 93.20%, and 97.40%, respectively. While increasing

catalyst loading provides more active sites to adsorb more dye molecules on catalyst surface, and react with dye initially, there may be some slow process, such as aggregation effects, in which too much of the catalysts slowly aggregate and restrict both light and dye molecules from accessing all of the available active sites in the catalysts.[18]

The effect of initial RhB concentration (20–150 mg L^{-1}) on the photocatalytic performance of CdS-4 was studied at a fixed solution pH of 3 and catalyst dose of 0.2 g, the result is displayed in Fig. 6b. It is observed that when the concentration of RhB is low (20 mg L^{-1}), the highest degradation speed can be achieved within 120 min. The rate of degradation decreases with the increase of initial RhB concentration, which is due to the blanket effect, the active sites of the catalyst surface are covered by more dye molecules so as to reduce the main active species.[55]

In a word, the optimal photocatalytic conditions are as follows: catalyst: CdS-4, catalyst dosage: 0.05 g, RhB concentration: 50 mg L^{-1}, pH: 3.0 and reaction time: 150 min.
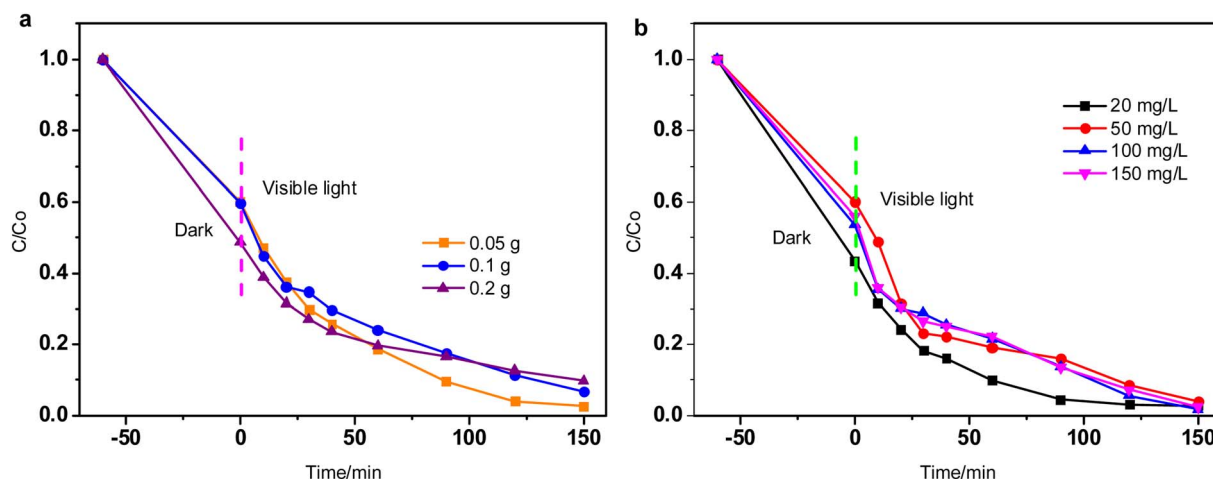

Fig. 6 Effect of catalyst dosage (a) and initial concentration of RhB (b) on photocatalytic performance.

3.2.4 Reusability of catalyst. One of the important indicators for evaluating the stability of catalyst is its reusability. Thus, CdS-4 was repeatedly used to degrade the RhB solution for seven times to evaluate its cycling stability, the result was displayed in Fig. 7. The removal efficiency of RhB is 99.60% after seven consecutive cycles. Apparently, based on the above result, this catalyst displays significant degradation activity and excellent reusability towards RhB elimination under visible light. The exceptional reusability of CdS-4 indicates its potential application in practical sewage treatment.

3.3. Possible mechanism of photocatalytic degradation

To further explore the photocatalytic process, the mechanism for photo-activated degradation of RhB was explored. To investigate the main reactive species generated in the visible light-generated photocatalytic degradation process, radical scavenging experiments were carried out using ethanol (EtOH), $AgNO_3$, tert-butyl alcohol (TBA), p-benzoquinone (BQ) as the quencher of hole (h^+), electron (e^-), hydroxyl radical ($^{\cdot}OH$) and superoxide radical anions ($^{\cdot}O_2^-$), respectively. As shown in Fig. 8a, the removal rate of RhB significantly decreases from 67.09% (blank) to 41.53% (EtOH), 52.77% ($AgNO_3$), 44.73% (TBA), 28.75% (BQ) with the addition of quencher. This result shows that the h^+, e^-, $^{\cdot}OH$ and $^{\cdot}O_2^-$ are the reactive oxidative species (ROS), the addition of quenchers hinder the photo-degradation of RhB. Among them, BQ shows the highest inhibition effect for RhB, indicating that $^{\cdot}O_2^-$ are the most important reactive species in photocatalytic reaction, and the h^+ plays a secondary role.

Fig. 8b displays the PL spectra (excitation at 390 nm) of the CdS and CdS-4 samples. The CdS sample shows a strong PL emission peak centered at about 765 nm, which is caused by the recombination of electron–hole pairs in the CdS. Once GQDs are added, the fluorescent intensity drops dramatically, and the main emission peak exhibits blue-shift to about 763 nm. The reduction of the fluorescent intensity can be attributed to lower charge recombination processes, indicating more efficient

separation of the electron–hole pair in CdS due to GQDs. This phenomenon suggests that improved yield of the charge-separated state of the CdS active site will enhance overall photocatalytic activity and organic pollutant degradation rates.

The efficient separation of the electron–hole pair over CdS-4 sample was further analysed by EIS, and compared with other GQDs/CdS samples. As shown in the EIS Nyquist plots results (Fig. 8c), the arc radius of CdS-4 is the smallest among these catalysts, implying that the highest charge-transfer capacity is presented in the interface between CdS-4 and electrolyte solution so as to effectively prevent the recombination of photo-produced electron–hole pairs, that is vital for enhanced photocatalytic efficiency, which is also in agreement with the results of PL and dye degradation.

To further characterize the radical species, EPR spectroscopy was performed to detect formation of either hydroxyl radicals ($^{\cdot}OH$) or superoxide radical anions ($^{\cdot}O_2^-$) produced by CdS-4 under visible light, using DMPO as trapping agent (Fig. 8d and e). DMPO can react with either radical species to generate a unique EPR signal that is diagnostic of either $^{\cdot}OH$ or $^{\cdot}O_2^-$ formation. Under dark conditions, no signals were observed, indicating that no ROS were produced by the CdS-4 catalyst without light irradiation. However, both samples show increasing signals with increasing illumination time from 1 min to 10 min. After 10 min of visible light irradiation, four peaks with relative peak heights of approximately $1:1:1:1$ can be observed (Fig. 8d), which are assigned to the DMPO–$^{\cdot}O_2^-$ peak, while four peaks with an intensity ratios of $1:2:2:1$ are ascribed to the formation of $^{\cdot}OH$ under illumination (Fig. 8e).[54] The very intense DMPO–$^{\cdot}O_2^-$ and DMPO–$^{\cdot}OH$ signals indicate that $^{\cdot}O_2^-$ and $^{\cdot}OH$ may both be involved in the visible light catalytic degradation.

The photo-adsorption effects of the catalyst was discussed. The photolysis and adsorption experiments were conducted in the same photocatalytic reaction instrument, the difference was that photocatalysis was carried out under visible light, while the adsorption process was in dark. The results show that RhB adsorption efficiency by CdS-4 reaches 46.5% after 10 min of dark adsorption, and the removal efficiency achieves 40.58% after 10 min of visible irradiation (Fig. 8f). The adsorption capacity in dark gradually decreases with the increase of adsorption time, which is due to desorption. While the degradation rate of dye is more than 74% under photocatalysis in 150 min. This catalyst exhibits good photocatalytic activity as well as adsorption capacity. Thus, RhB dye is removed not only by ROS, but also by synergistic adsorption-photocatalysis process.

Based on these results, a possible mechanism for photocatalytic degradation by CdS-4 under visible light is proposed in Fig. 9. First, visible light initiates photoexcitation of the CdS-4 to generate electrons and holes, and the high energy react with O_2 in solution to form $^{\cdot}O_2^-$. Next, $^{\cdot}O_2^-$ reacts with H^+ and e^- to produce H_2O_2, H_2O_2 then captures electrons from step (3) to form $^{\cdot}OH$. These ROS then can effectively degrade the RhB dye. During this process, the GQDs can provide a rapid electron transfer pathway to reach efficient charge separation.[24] GQDs mainly act as electron acceptor instead of a photosensitizer in
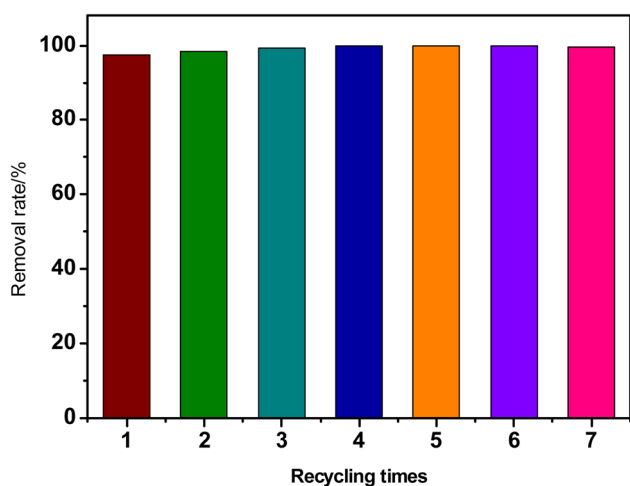

Fig. 7 Reusability tests on degradation of RhB by CdS-4 (conditions: pH 3.0, dosage: 0.05 g, initial concentration: 50 mg L^{-1}).
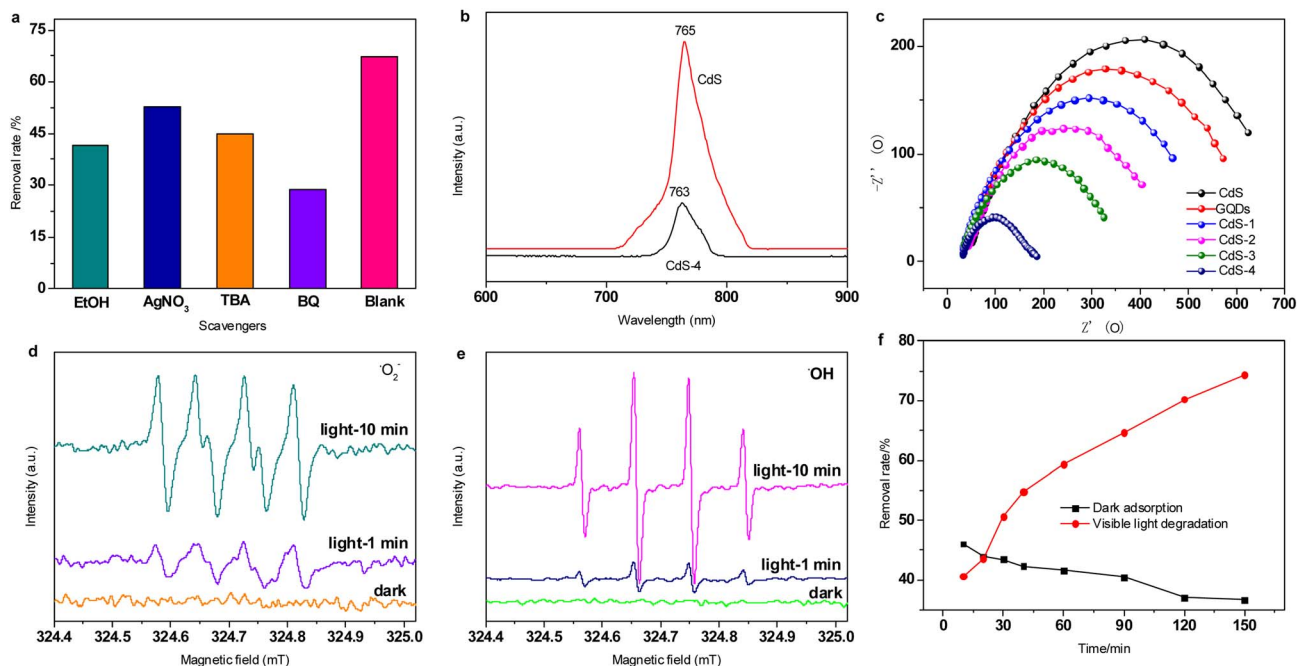
Fig. 8 (a) Removal rate of RhB in the presence of different scavengers (the catalyst dose: 0.02 g, RhB: 50 mg L^{-1}, pH = 7.0), (b) PL spectrum of CdS and CdS-4, (c) EIS Nyquist plots of CdS, GQDs and GQDs/CdS with different GQDs loading, (d) ESR spectra of DMPO−$^{\cdot}$O$_2^-$ and (e) DMPO−$^{\cdot}$OH for CdS-4 under dark or visible light irradiation, (f) photo-adsorption experiment over CdS-4 (the catalyst dose: 0.03 g, RhB: 50 mg L^{-1}, pH = 7.0).
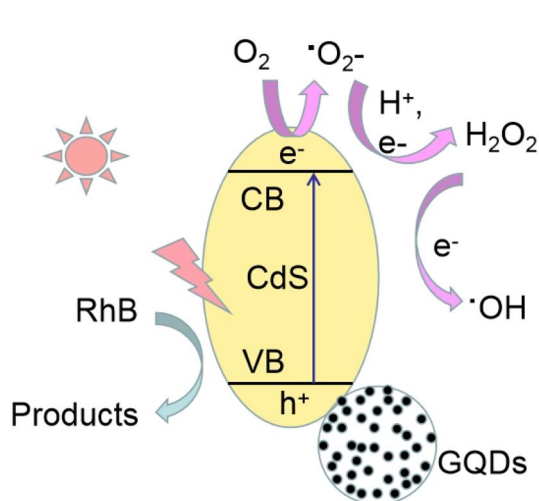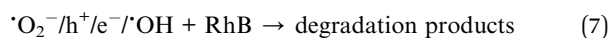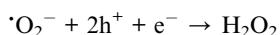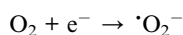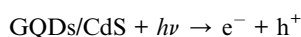

Fig. 9 Photocatalytic mechanism of RhB degradation by GQDs/CdS under visible light irradiation.

improving photocatalytic performances of GQDs/CdS.[24] The overall chemical reaction of the photocatalytic degradation of RhB can be inferred as follows:

$$GQDs/CdS + h\nu \rightarrow e^- + h^+ \tag{3}$$

$$O_2 + e^- \rightarrow {}^{\cdot}O_2^- \tag{4}$$

$${}^{\cdot}O_2^- + 2h^+ + e^- \rightarrow H_2O_2 \tag{5}$$

$$H_2O_2 + e^- \rightarrow {}^{\cdot}OH + OH^+ \tag{6}$$

$${}^{\cdot}O_2^-/h^+/e^-/{}^{\cdot}OH + RhB \rightarrow degradation\ products \tag{7}$$

4. Conclusion

In summary, a GQDs/CdS catalyst was prepared *via* solvothermal and hydrothermal deposition and applied to degrade RhB dye. The photocatalytic activity of CdS was significantly improved by coupling with GQDs. The UV-vis diffuse reflectance and PL spectrum of GQDs/CdS showed excellent visible-light absorption properties and high electron–hole separation efficiency. The best degradation rate was achieved with CdS-4, and 0.05 g catalyst at pH 3. Then, radical trap experiments found evidence for h$^+$, e$^-$, $^{\cdot}$OH and $^{\cdot}$O$_2^-$ as the main reactive species, RhB dye was removed *via* reactive oxidative species and synergistic adsorption-photocatalysis process. Finally, we have taken these results to propose a mechanistic model for the photodegradation of RhB by CdS-4.

Author contributions

X. L. and M. C. contributed equally to conceptualization, investigation, methodology, resources, formal analysis, writing-original draft, and writing, review and editing; funding acquisition conceptualization, review and supervision. Y. C., D. Z. and H. G. contributed investigation, methodology, writing – original draft, writing – review & editing. W. L. contributed investigation and methodology.

Conflicts of interest

The authors declare no conflicts.

Acknowledgements

References

1 K. Tsuchid, H. Okumura, T. Ikarashi and Y. Takahashi, *J. Photochem. Photobiol., A*, 2022, **433**, 114163.

2 S. Keerthana, R. Yuvakkumar, G. Ravi, M. Manimegalai, M. Pannipara, A. G. Al-Sehemi, R. A. Gopal, M. M. Hanafiah and D. Velauthapillai, *Environ. Res.*, 2021, **199**, 111312.

3 M. Ahmad, M. T. Qureshi, W. Rehman, N. H. Alotaibi, A. Gul, R. S. A. Hameed, M. A. E. Elaimi, M. F. H. Abdel-kader, M. Nawaz and R. Ullah, *J. Alloys Compd.*, 2022, **895**, 162636.

4 M. Danish and M. Muneer, *Ceram. Int.*, 2021, **47**, 13043–13056.

5 A. Ghafoor, I. Bibi, S. Ata, F. Majid, S. Kamal, M. Iqbal, S. Iqbal, S. Noureen, B. Basha and N. Alwadai, *J. Mol. Liq.*, 2021, **343**, 117581.

6 G. E. Ezzatpour, W. Marc and W. I. Richard, *Dalton Trans.*, 2023, **52**, 11143–11157.

7 E. N. Zare, S. Iftekhar, Y. Park, J. Joseph, V. Srivastava, M. A. Khan, P. Makvandi, M. Sillanpaa and R. S. Varma, *Chemosphere*, 2021, **280**, 130907.

8 M. M. Gul and K. S. Ahmad, *Rev. Inorg. Chem.*, 2021, **42**(4), 337–354.

9 A. G. Akerdi and S. H. Bahrami, *J. Environ. Chem. Eng.*, 2019, **7**, 103283.

10 J. Fu, J. Yu, C. Jiang and B. Cheng, *Adv. Energy Mater.*, 2018, **3**, 1701503.

11 R. Guo, J. Wang, Z. Bi, X. Chen, X. Hu and W. Pan, *Chemosphere*, 2021, **295**, 133834.

12 X. Fan, S. Zhang, R. Guan, X. Shao, S. Jiang, Y. Hu, S. Wang and Q. Yu, *J. Mol. Struct.*, 2022, **1252**, 132163.

13 A. Khan, Z. Rehman, A. Khan, H. Ambareen, H. Ullah, S. M. Abbas, Y. Khan and R. Khan, *Inorg. Chem. Commun.*, 2017, **79**, 99–103.

14 S. Y. Janbandhu, C. T. Suhaila, S. R. Munishwar, J. R. Jayaramaiah and R. S. Gedam, *Chemosphere*, 2022, **286**, 131672.

15 X. Xu, L. Hu, N. Gao, S. Liu, S. Wageh, A. A. Al-Ghamdi, A. Alshahrie and X. Fang, *Adv. Funct. Mater.*, 2015, **25**, 445–454.

16 T. Fan, Y. Li, J. Shen and M. Ye, *Appl. Surf. Sci.*, 2016, **367**, 518–527.

17 Y. Lin, D. Tsai, Z. Chang and F. Shieu, *Appl. Surf. Sci.*, 2018, **440**, 1227–1234.

18 F. Jiang, T. Yan, H. Chen, A. Sun, C. Xu and X. Wang, *Appl. Surf. Sci.*, 2014, **295**, 164–172.

19 N. Kumar and V. Dutta, *Appl. Surf. Sci.*, 2014, **288**, 172–179.

20 N. Bao, L. Shen, T. Takata and K. Domen, *Chem. Mater.*, 2008, **20**, 110–117.

21 J. Yu, Y. Yu and B. Cheng, *RSC Adv.*, 2012, **2**, 11829–11835.

22 Y. Guo, J. Wang, Z. Tao, F. Dong, K. Wang, X. Ma, P. Yang, P. Hu, Y. Xu and L. Yang, *CrystEngComm*, 2012, **14**, 1185–1188.

23 A. C. Kuriakose, V. Nampoori and S. Thomas, *Mater. Chem. Phys.*, 2021, **258**, 123911.

24 Y. Lei, C. Yang, J. Hou, F. Wang, S. Min, X. Ma, Z. Jin, J. Xu, G. Lu and K. Huang, *Appl. Catal., B*, 2017, **216**, 59–69.

25 F. Wang, Y. Liao, T. Li and L. Xi, *Sep. Purif. Technol.*, 2022, **299**, 121707.

26 H. Xia, X. Xu and D. Li, *J. Alloys Compd.*, 2022, **914**, 165393.

27 X. Li, A. Xu, H. Fan, X. Liu, J. Wang, J. Cao, L. Yang and M. Wei, *J. Power Sources*, 2022, **545**, 231923.

28 H. Fu, H. Zhao, X. Yang, S. Xiong and X. An, *Powder Technol.*, 2022, **406**, 117596.

29 H. Qiu, X. Qu, X. Zhang, S. Chen and Y. Shen, *Adv. Mater.*, 2023, **35**, 2302326.

30 T. Zhang, W. Li, K. Huang, H. Guo, Z. Li, Y. Fang, R. M. Yadav, V. Shanov, P. M. Ajayan, L. Wang, C. Lian and J. Wu, *Nat. Commun.*, 2021, **12**, 5265.

31 I. Ibrahim, H. Lim, N. Huang, Z. Jiang and M. Altarawneh, *J. Hazard. Mater.*, 2020, **391**, 122248.

32 C. Wang, S. Li, M. Cai, R. Yan, K. Dong, J. Zhang and Y. Liu, *J. Colloid Interface Sci.*, 2022, **619**, 307–321.

33 L. Zhou, H. Guo, Z. Wang and L. Wang, *Carbon*, 2023, **213**, 118249.

34 M. Fan, Z. Wang, K. Sun, A. Wang, Y. Zhao, Q. Yuan, R. Wang, J. Raj, J. Wu, J. Jiang and L. Wang, *Adv. Mater.*, 2023, **35**, 2209086.

35 C. Santos, L. Rodríguez-Perez, G. Gonçalves, S. Pinto, M. Melle-Franco, P. Marques, M. Faustino, M. Herranz, N. Martin, M. Neves, J. Martinho and E. Maçoas, *Carbon*, 2020, **166**, 164–174.

36 H. Zhang, J. Gu, Y. Zhang, H. Guo, S. Zhang, J. Song, C. Liu, L. Wang, D. Li and B. Dai, *ACS Nano*, 2023, **17**, 10129–10141.

37 R. Yadav, Z. Li, T. Zhang, O. Sahin, S. Roy, G. Gao, H. Guo, R. Vajtai, L. Wang, P. M. Ajayan and J. Wu, *Adv. Mater.*, 2022, **34**, 2105690.

38 Y. Huang, J. Zhang, K. Dai, C. Liang and G. Dawson, *Ceram. Int.*, 2022, **148**, 8423–8432.

39 V. Kumar, N. Singh, S. Jana, S. K. Rout, R. K. Dey and G. P. Singh, *Int. J. Hydrogen Energy*, 2021, **46**, 16373–16386.

40 Z. Zhang, M. Wang, H. Zhou and F. Wang, *J. Am. Chem. Soc.*, 2021, **143**, 6533–6541.

41 S. Min, J. Hou, Y. Lei, X. Ma and G. Lu, *Appl. Surf. Sci.*, 2017, **396**, 1375–1382.

42 Y. Sun, X. Yuan, Y. Wang, W. Zhang, Y. Li, Z. Zhang, J. Su, J. Zhang and S. Hu, *Appl. Surf. Sci.*, 2022, **576**, 151901.

43 F. Nekouei, S. Nekouei, M. Pouzesh and Y. Liu, *Chem. Eng. J.*, 2020, **385**, 123710.

44 F. Nekouei, S. Nekouei and H. Kargarzadeh, *Chem. Eng. J.*, 2018, **335**, 567–578.

45 X. Shen, Z. Wang, H. Guo, Z. Lei, Z. Liu and L. Wang, *Small*, 2023, 2303156.

46 H. Wu, J. Ding, D. Yang, J. Li, Y. Shi and Y. Zhou, *Ceram. Int.*, 2020, **146**, 17800–17808.

47 Z. Wang, G. Li, W. Hou, H. Guo, L. Wang and M. Wu, *ACS Nano*, 2023, **17**, 8671–8679.

48 H. Choi, W. Chen and P. Kamat, *ACS Nano*, 2012, **6**(5), 4418–4427.

49 J. Chen, J. Wu, P. Wu and D. Tsai, *J. Phys. Chem. C*, 2011, **115**(1), 210–216.

50 Y. Xue, Q. Chang, X. Hu, J. Cai and H. Yang, *J. Environ. Manage.*, 2020, **274**, 111184.

51 X. Wang, Y. Li and S. Yi, *Acta Mater. Compositae Sin.*, 2022, **39**(8), 3845–3851.

52 F. Chen, J. Zhao and H. Hidaka, *Int. J. Photoenergy*, 2003, **5**, 209–217.

53 C. Zhao, Y. Chen, C. Li, Q. Zhang, P. Chen, K. Shi, Y. Wu and Y. He, *J. Phys. Chem. Solids*, 2020, **136**, 109122.

54 Y. Wang, C. Yang, Y. Zhang, L. Guo, Y. Wang, G. Gao, F. Fu, B. Xu and D. Wang, *Int. J. Hydrogen Energy*, 2022, **47**, 9566–9578.

55 N. Kumari, S. Chintakula, I. Anantha and S. Maddila, *Results Chem.*, 2023, **5**, 100759.